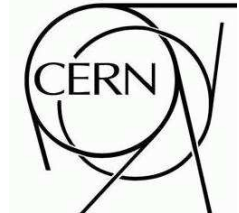# ATLAS NOTE

May 9, 2008

Electroweak boson cross-section measurements with ATLAS

The ATLAS Collaboration

Abstract

This report summarises the ATLAS prospects for the measurement of W and Z production cross-section at the LHC. The electron and muon decay channels are considered. Focusing on the early data taking phase, strategies are presented that allow a fast and robust extraction of the signals. In the W channels, a measurement precision of about 5% can be achieved with 50 pb^{-1}. The uncertainty is dominated by the background uncertainty. In the Z channels, the expected precision is 3%, the main contribution coming from the lepton selection efficiency uncertainty. Extrapolating to $\mathscr{L} = 1\text{fb}^{-1}$, the uncertainties shrink to incompressible values of 1-2%, depending on the final state. This irreducible uncertainty is essentially driven by strong interaction effects, notably PDF uncertainties and non-perturbative effects, affecting the W and Z rapidity and p_T distributions. These effects can be constrained by measuring these distributions. Algorithms allowing the extraction of the Z differential cross-section are presented accordingly.

1 W and Z cross-section measurements at the LHC

The study of the production of *W* and *Z* events at the LHC is fundamental in several respects. At first, the calculation of higher order corrections to these simple, colour singlet final states is very advanced, with a residual theoretical uncertainty smaller than 1%. Such precision makes *W* and *Z* production a stringent test of QCD.

Secondly, more specifically for *Z* production, the clean and fully reconstructed leptonic final states will allow a precise measurement of the distributions ($d\sigma/dp_T$, $d\sigma/dy$). The transverse momentum distribution will provide more constraints on QCD, most significantly on non-perturbative aspects related to the resummation of initial parton emissions, while the rapidity distribution is a direct probe of the parton density functions (PDFs) of the proton. The high expected counting rates will bring significant improvement on these aspects, and this improvement translates to virtually all physics at the LHC, where strong interaction and PDF uncertainties are a common factor.

From the experimental point of view, the precisely measured properties of the *Z* boson provide strong constraints on the detector performance. Its mass, width and leptonic decays can be exploited to measure the detector energy and momentum scale, its resolution, and lepton identification efficiency very precisely.

Finally, a number of fundamental electroweak parameters can be accessed through *W* and *Z* final states (M_W, through the *W* boson decay distributions; $\sin^2\theta_W$, via the *Z* forward-backward asymmetry; lepton universality, by comparing electron and muon cross-sections). These measurements are long term applications where the understanding of the hadronic environment at the LHC is crucial, and to which the above-mentioned measurements are necessary inputs.

The present note summarises the ATLAS preparations for *W* and *Z* cross-section measurements, in the context of the early running of ATLAS and the LHC. The electron and muon decay channels are considered. A baseline luminosity of $\mathcal{L} = 50$ pb^{-1} is assumed for the total cross-section analyses; based on these results, we estimate our prospects for $\mathcal{L} = 1$ fb^{-1}. Anticipating that the measurement precision will soon be limited by the above-mentioned theoretical uncertainties, differential cross-section analyses are presented in the second part of this work. We consider the Drell-Yan mass spectrum below the *Z* peak, and *y* and p_T distributions on the *Z* resonance.

The note is organised as follows. Section 2 gives technical details about cross-section measurements, lists the simulation samples used in the analyses, and reminds the main reconstruction aspects. Sections 3 and 4 describe the selections that allow to extract the *W* and *Z* signals, give the expected statistics, and discuss the uncertainties on the background rates, as these are specific to each channel. Common systematic uncertainties affecting the cross-section determination are discussed in Section 5. Section 6 then presents the expected performance for total cross-section measurement. Differential cross-sections are discussed in Section 7, and Section 8 summarizes our results.

2 General discussion

This section describes the general procedure used to extract physical cross-sections, and the simulation samples used to evaluate the expected performance.

2.1 Cross-section measurements

The number of events N passing a given set of selections is expressed as follows:

$$N = \mathscr{L} \, \sigma \, A \, \varepsilon + B \tag{1}$$

where $\mathscr{L}$ is the integrated luminosity; σ the signal cross-section; A the acceptance of the signal, defined as the fraction of the signal that passes the kinematic and angular cuts; ε is the reconstruction efficiency of the signal within the fiducial acceptance; B is the number of background events. In the above, ε is to be understood as averaged over the phase space accepted by the selections. Conversely, the measured cross-section is expressed as:

$$\sigma = \frac{N - B}{\mathscr{L} \, A \, \varepsilon} \tag{2}$$

and the total measurement uncertainty gets contributions from the different terms as below:

$$\frac{\delta \sigma}{\sigma} = \frac{\delta N \oplus \delta B}{N - B} \oplus \frac{\delta \mathscr{L}}{\mathscr{L}} \oplus \frac{\delta A}{A} \oplus \frac{\delta \varepsilon}{\varepsilon} \tag{3}$$

Above, $\delta N \sim \sqrt{N}$ is of purely statistical origin, and the relative uncertainty decreases with increasing luminosity following $\delta N / N \sim 1/\sqrt{\mathscr{L}}$. The terms δB, δA and $\delta \varepsilon$ are of both theoretical and experimental origin. They are considered as systematic uncertainties in the cross-section measurements, but can be constrained *via* auxiliary measurements. We thus expect these terms to improve over time, provided the auxiliary measurements have statistically dominated uncertainties. $\delta \mathscr{L}$ is given externally and decreases only through improved understanding of the LHC.

2.2 Signal and background samples. Benchmark cross-sections

Our main signals, W and Z events decaying into electrons and muons, are generated using `PYTHIA` [1]. The analysis described in Section 7, a measurement of the low-mass Drell-Yan cross-section, also exploits samples produced using `PYTHIA`.

The W and Z samples are filtered at generation-level, requiring at least one lepton within the fiducial acceptance. The electron channels require $|\eta_e| < 2.7$ and $p_T^e > 10$ GeV; the muon channels require $|\eta_\mu| < 2.8$ and $p_T^\mu > 5$ GeV. These filters have an efficiency of about 85% depending on the final state. The available energy for the hard process is limited by $\sqrt{\hat{s}} > 60$ GeV. The low-mass Drell-Yan samples have the same fiducial cuts, but require $10 < \sqrt{\hat{s}} < 60$ GeV. The Drell-Yan, W and Z cross-sections are normalised to the NNLO cross-sections as provided by the `FEWZ` program [2].

The backgrounds considered in the analyses originate from W and Z events decaying to τ-leptons, with subsequent leptonic τ decays; $t\bar{t}$ events involving at least one semileptonic decay, and from inclusive jet events filtered to favour the presence of real leptons or hadrons misidentified as leptons. The $W \to \tau \nu_\tau$ and $Z \to \tau \tau$ events are produced as the signal samples. The $t\bar{t}$ samples are generated using `MC@NLO` [3] to provide both the final states and the cross-section.

The jet events are produced again using `PYTHIA`. Jet backgrounds for the muon channels are generated as inclusive jets, then requiring a final state with one (W analysis; $p_T(\mu) > 15$ GeV) or two (Z analysis; $p_T(\mu) > 5$ and 15 GeV) muons from b-hadron decays with $|\eta_\mu| < 2.5$. Background events from hadron punch-through and from decays in flight of long lived particle were found negligible.

Background events from cosmic muons can be eliminated in a very efficient way with timing cuts. Relying on the Tevatron results, this background was neglected. This appears as a safe approximation for the ATLAS experiment, since the Tevatron experiments are built close to the surface, while the ATLAS detector is ~ 100 m underground. In the electron channels, fake electrons are an important issue. Therefore, rather than requiring a true electron in the final state, the events are required to contain at least one narrow cluster of energetic final state particles. In practice, there should exist a cone of size $\Delta\eta \times \Delta\phi = 0.12 \times 0.12$ containing a total transverse energy greater than 17 GeV. Events passing this filter are considered likely to produce fake electrons and passed through the simulation step.

In the low-mass Drell-Yan analysis, the background from diboson production is generated using `MC@NLO` (WW and ZZ events) and Herwig (WZ events).

All samples are interfaced to the CTEQ6M parton density sets [5], and processed through full simulation using Geant 6.4 and a special misaligned geometry, as described in [6]. While reminded here, the cross-sections used are described and justified, together with their uncertainties, in [7]. Tables 1 and 2 summarise the signal and background samples and their properties.

Channel	σ_{tot}	ε_{filter}	N_{evt} ($\times 10^3$)	$\mathscr{L}$ (pb^{-1})
$W \to e\nu$	20510 pb	0.63	140	11
$Z \to ee$	2015 pb	0.86	399	230
$(\gamma/Z)* \to ee$	9220 pb	0.126	331	284
$W \to \tau\nu_\tau$	20510 pb	0.20	32	8
$Z \to \tau\tau$	2015 pb	0.05	13	129
$t\bar{t}$	833 pb	0.54	382	850
Inclusive jets	2333 μb	0.09	3725	0.02
WW	1.275 pb	1.	20	15608
ZZ	14.8 pb	1.	43	2922
WZ	27.0 pb	0.29	48	6141

Table 1: Signals and background samples in the electron channels. *W* and *Z* cross-sections are normalised to the NNLO prediction; the $t\bar{t}$ cross-section is computed at NLO; the jet cross-section is the LO result. The filters are described in the text.

2.3 Common selection aspects

As already mentioned, *W* and *Z* boson final states are selected through their decays into electrons and muons. The reconstruction of electrons is based on a cluster measured in the electromagnetic calorimeter, geometrically matching a track reconstructed in the Inner Detector. The identification of isolated high-p_T electrons is then based on the shapes of the electromagnetic showers, and on track reconstruction information. Three sets of identification criteria have been defined. The Loose criterion consists of simple shower-shape cuts; the Medium criterion adds further cuts on shower-shape and on track quality; the Tight criterion tightens the track-matching requirement, adds a cut on the energy-momentum ratio and further selections based on the vertexing-layer hits and on the Transition

Channel	σ_{tot}	ε_{filter}	N_{evt} ($\times 10^3$)	$\mathscr{L}$ (pb^{-1})
$W \to \mu\nu$	20510 pb	0.69	190	13
$Z \to \mu\mu$	2015 pb	0.89	446	249
$W \to \tau\nu_\tau$	20510 pb	0.20	32	8
$Z \to \tau\tau$	2015 pb	0.05	13	129
$t\bar{t}$	833 pb	0.54	382	850
$b\bar{b} \to \mu + X$	766 μb	2.1×10^{-4}	110	0.67
$b\bar{b} \to \mu\mu + X$	25 μb	1.6×10^{-4}	140	35

Table 2: Signals and background samples in the muon channels. W and Z cross-sections are normalised to the NNLO prediction; the $t\bar{t}$ cross-section is computed at NLO; the $b\bar{b}$ cross-section is the LO result. The filters are described in the text.

Radiation Tracker. Electron reconstruction and its performance are described in [8].

The muon reconstruction is done with the Muon Spectrometer, possibly completed by the Inner detector. Stand-alone muons are defined as consisting of a reconstructed track in the spectrometer only, and combined muons are the subset of the above that include a matching track in the Inner Detector. Muon reconstruction is documented in [9].

The measurement of missing energy in the transverse plane ($\not{E}_T$) is an important requirement for W boson cross-section measurements, as significant $\not{E}_T$ reflects the presence of at least one neutrino in the final state. The algorithm exploits the energy deposits in the calorimeter cells, the reconstructed muon tracks, and an estimate of the energy lost in the cryostat. The calorimeter cells are calibrated according to the physical object they represent (electrons or photons, taus, jets and muons). Cells corresponding to electrons, photons and muons are calibrated at the electromagnetic scale, whereas all other cells are calibrated at the hadronic scale. The $\not{E}_T$ value is then computed as the vector sum of the cell transverse energies. If muons are reconstructed in the event, their transverse momentum is added to the calorimetric sum. A complete description of the $\not{E}_T$ reconstruction can be found in [10].

Jets are reconstructed from calorimeter cells. The Cone algorithm is used, where the jet size parameter, $\Delta R = \sqrt{\Delta\eta^2 + \Delta\phi^2}$, is set to $\Delta R = 0.7$.

At low luminosity, $\mathscr{L} = 10^{31}$ cm^{-2}s^{-1}, the relevant trigger items require at least one electron or muon with p$_T$ > 10 GeV, at least two electrons with p$_T$ > 5 GeV, or two muons with p$_T$ > 4 GeV. No isolation criteria are imposed on the leptons. As the LHC luminosity ramps up towards its design value, tighter selections will be needed to control the rates. The thresholds are raised, and isolation criteria are imposed on the electrons. The trigger items relevant for W boson selection now require at least one isolated electron with p_T > 22 GeV, or one muon with p_T > 20 GeV. For Z production, two isolated electrons with p_T > 12 GeV or two muons with p_T > 10 GeV can be required in addition to the above. The trigger items described above are reminded in Table 3. Many more trigger items exist; a complete description can be found in [11, 12].

The reconstruction efficiency for electrons and muons, and the resolution of the $\not{E}_T$ reconstruction algorithm are illustrated in Fig. 1. For electrons, the Medium identification efficiency is illustrated,

Trigger item	Description
e10, e20	One electron, $p_T > 10, 20$ GeV
mu10, mu20	One muon, $p_T > 10, 20$ GeV
2e5	Two electrons, $p_T > 5$ GeV
2mu4	Two muons, $p_T > 4$ GeV
e22i	One isolated electron, $p_T > 22$ GeV
mu20	One isolated muon, $p_T > 20$ GeV
2e12i	Two isolated electrons, $p_T > 12$ GeV
2mu10	Two isolated muons, $p_T > 10$ GeV

Table 3: Main trigger items relevant for the selection of W and Z boson final states. The first group of trigger items is relevant to the $\mathscr{L} = 10^{31}$ cm^{-2}s^{-1} trigger menu; the second group is relevant for the $\mathscr{L} = 10^{33}$ cm^{-2}s^{-1} trigger menu.

and the muon combined reconstruction efficiency is shown. With looser criteria, higher efficiency and weaker η dependence are obtained, at the cost of larger backgrounds. A complete description of the ATLAS detector and its performance can be found in [13].
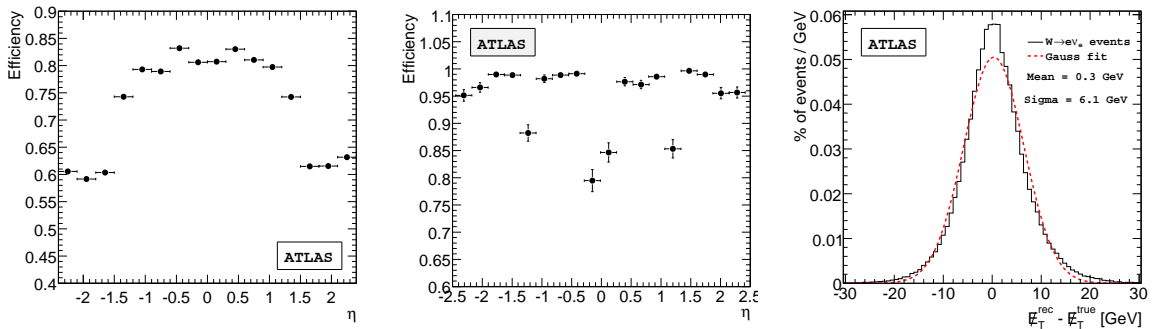

Figure 1: From left to right : Electron Medium identification efficiency vs. η; muon combined reconstruction efficiency vs. η; $\not{E}_T$ resolution. The efficiencies are obtained from Z boson events, and integrated over $p_T > 20$ GeV. The $\not{E}_T$ resolution is obtained from $W \to e\nu$ events.

3 Electron final states

This section describes the event selections in the electron final states, the expected event rates, and estimations of the uncertainties on the remaining backgrounds.

3.1 $W \to e\nu$

Event selection. The selection of $W \to e\nu$ events proceeds as follows. First, the e20 trigger item of the 10^{31} trigger menu should be passed. Then, exactly one electromagnetic (EM) cluster, matched with a track and such that $E_T > 25$ GeV, $| \eta | < 1.37$ or $1.52 < | \eta | < 2.4$, should be present in the event. This object should satisfy the Medium electron identification criterion. Finally, the reconstructed

Selection	$W \to e\nu$	jets	$W \to \tau\nu$	$Z \to ee$
Trigger	37.01 ± 0.09	835 ± 18	1.73 ± 0.02	6.07 ± 0.01
$p_T > 25$ GeV, $|\eta| < 2.4$	30.84 ± 0.09	383 ± 12	1.03 ± 0.01	2.95 ± 0.01
Electron ID	26.77 ± 0.09	110 ± 6	0.91 ± 0.01	3.23 ± 0.01
$\not{E}_T > 25$ GeV	22.06 ± 0.09	4.6 ± 0.7	0.55 ± 0.01	0.06 ± 0.01
$M_T > 40$ GeV	21.71 ± 0.08	1.5 ± 0.4	0.43 ± 0.01	0.04 ± 0.01

Table 4: Number of expected signal and background events ($\times 10^4$) in the $W \to e\nu$ channel after all selections, for an integrated luminosity of 50 pb^{-1}. The quoted uncertainties refer to the finite Monte-Carlo statistics only; systematic uncertainties are discussed in the text.
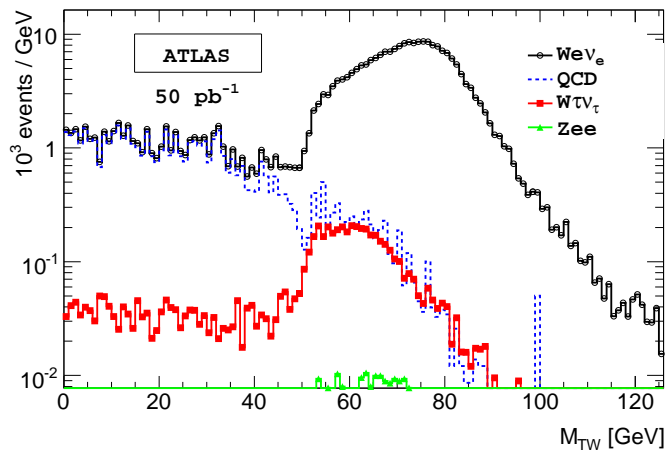

Figure 2: Transverse mass distribution in the $W \to e\nu$ channel, for signal and background after all selections, for $\mathscr{L} = 50$ pb^{-1}.

missing transverse energy, reflecting the missing final state neutrino, should satisfy $\not{E}_T > 25$ GeV, and the transverse mass of the (l, ν) system should satisfy $M_T > 40$ GeV.

Due to the high di-jet cross-section and the high rejection power of the selections, the available Monte Carlo statistics is not sufficient to evaluate this background directly. To overcome this difficulty, the jet background has been estimated by applying the trigger and electron identification selections only, and correcting the result with a factor obtained by computing the rejection power due to the $\not{E}_T$ and M_T cuts only.

The number of signal and background events after the successive cuts are given in Table 4 for an integrated luminosity of 50 pb^{-1}. The expected number of signal events is is $N_S = (21.71 \pm 0.04) \times 10^4$ events (the uncertainty given here is related to the data sample size; the uncertainty given in Table 4 comes from the finite size of the simulation sample). The resulting transverse mass distribution is shown in Fig. 2.

Background estimation. As can be seen from Table 4, jet events constitute the largest background component. In addition, the jet production cross-section and fragmentation properties at the LHC
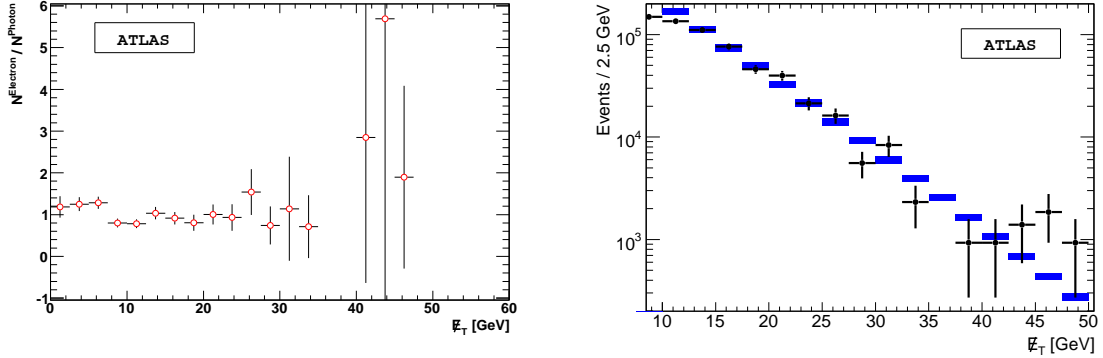
Figure 3: Left: ratio of the $\not{E}_T$ distributions in jet background events and in the control sample. Right: comparison of the jet background (points with error bars) and the fitted background (rectangles), for an integrated luminosity of 50 pb^{-1}.

are largely unknown and induce a significant uncertainty on the magnitude of this background; an uncertainty of about a factor 3 is estimated. It is therefore important to develop methods allowing to monitor the jet background using the data. An attempt is presented below.

The principle of the method is to measure the normalisation and shape of the jet background ahead of the $\not{E}_T$ cut, in a sufficiently pure jet sample. It is thus needed to find a jet sub-sample that is free of signal events, but exhibits a transverse mass distribution and jet multiplicity close to that of the jet background to $W \to e\nu$ at this level of the selection. This sub-sample is then used to evaluate the rejection of $\not{E}_T$ cut, allowing a realistic estimation of the jet background in the $W \to e\nu$ selection.

In this approach, the signal sample is obtained by applying the same trigger, kinematics and electron identification selection as described before and removing in addition events with a second high-p_T electromagnetic cluster giving an invariant mass, together with first selected electron, close to the Z boson mass ($65 < M < 130$ GeV).

The jet background control sample is selected using a single photon trigger with $E_T > 20$ GeV, and subsequent photon identification using the same calorimetric variables as the electron identification. The photon cluster should also satisfy the same kinematics cuts of the electron candidate in the signal sample. There should be no Inner Detector track matching the photon cluster, to reject events with true electrons (e.g. W events) contaminating this photon sample. Simulation studies show that these selections provide a sample essentially composed of jet events, even at high values of $\not{E}_T$, and that the shape of the $\not{E}_T$ distribution is identical, within the statistical precision, to that of the jet background in the $W \to e\nu$ sample (see Fig. 3). Above $\not{E}_T > 10$ GeV, the slope can be described with the convolution of an exponential and a second degree polynomial function.

After the subtraction of the estimated background to the signal sample, the analysis then proceeds applying the $\not{E}_T$ selection mentioned above. This data-driven estimation yields a jet background fraction of $(0\pm4)\%$. In terms of number of events, $\delta B = 0.92 \times 10^4$ events. Besides, a relative uncertainty of 3% is assumed on the $W \to \tau\nu$ background, as estimated from the experimental uncertainties on the W and τ branching fractions. This process thus contributes $\delta B = 0.01 \times 10^4$ events.
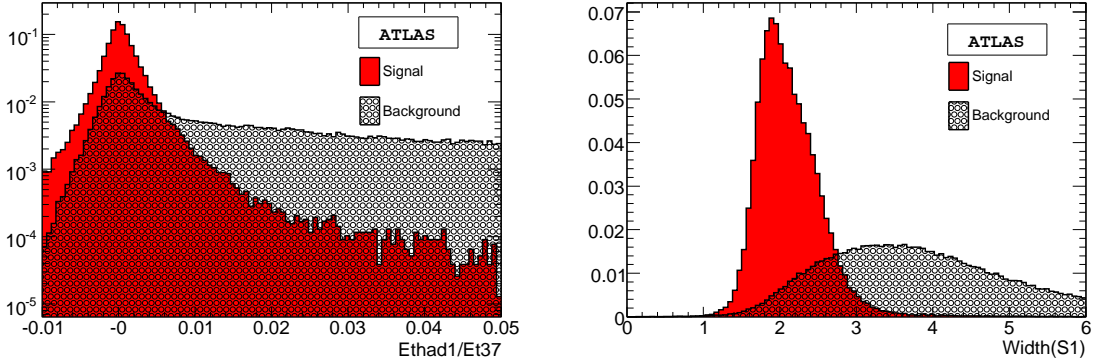
8

Figure 4: The electron identification criteria described in the text: the cluster hadronic to EM energy ratio (left); the cluster width in the first calorimeter sampling (right). The distributions are normalised to the number of background entries.

3.2 $Z \to ee$

Event selection. This analysis relies on the e10 trigger. Events are further preselected by requiring two EM clusters with $E_T > 15$ GeV and $|\eta| < 2.4$. The presence of two electrons in the final state allows to apply the Loose electron identification criteria, which we briefly describe below. Three discriminant variables are used to separate EM clusters, deposited by electrons, from the hadronic background.

The first one is based on the longitudinal shower shape, and represents the ratio of the transverse energy deposited in the first compartment of the hadronic calorimeter divided by the transverse energy of the EM cluster. This ratio is expected to be small for EM objects, and large for hadronic clusters.

The second and third one are based on the shower width measured in the EM calorimeter. In the second compartment of the EM calorimeter, the width is computed from the ratio of the shower energy deposited in a region of size $\Delta\eta \times \Delta\phi = 0.075 \times 0.175$, divided by the energy deposited within $\Delta\eta \times \Delta\phi = 0.175 \times 0.175$ around the cluster barycenter. In the first compartment, the cluster spread is used, computed as the root-mean-square (RMS) of cluster the energy distribution. These two variables discriminate the narrow EM clusters from the wider hadronic clusters. Distributions of the three discriminators for electrons and hadrons are shown in Fig. 4 and in Fig. 5.

Electrons identified as above are then required to be isolated. The isolation variable is computed from the total measured energy in a cone of size $\Delta R = 0.45$ around and excluding the electron, divided by the electron energy. Electrons are isolated if this ratio is smaller than 0.2. Distributions of this variable for the signal and the background are shown in Fig. 5.

The number of signal and background events after the successive cuts are given in Table 5 for an integrated luminosity of 50 pb^{-1}. The expected signal counting rate is $N = (2.48 \pm 0.02) \times 10^4$ events (the uncertainty given here is related to the data sample size). The resulting di-electron invariant mass distribution is shown in Fig. 6.
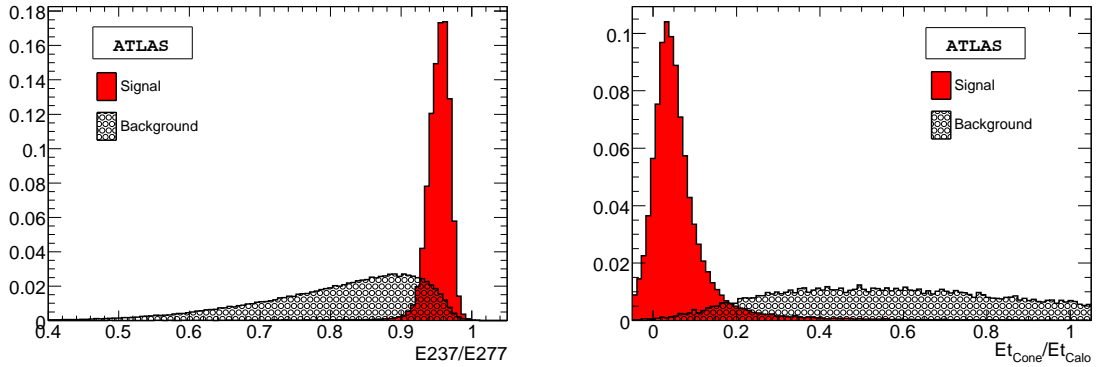
9

Figure 5: The electron identification criteria described in the text: cluster width in the second calorimeter sampling (left) and electron isolation variable (right).The distributions are normalised to the number of background entries.

Selection	$Z \to ee$	jets
Trigger	6.70 ± 0.01	3110 ± 40
$p_T > 15\,\mathrm{GeV}$, $\lvert \eta \rvert < 2.4$, $80\,\mathrm{GeV} < M_{ee} < 100\mathrm{GeV}$	2.76 ± 0.01	11.1 ± 0.8
Electron ID	2.64 ± 0.01	0.8 ± 0.2
Isolation	2.48 ± 0.01	0.2 ± 0.1

Table 5: Number of expected signal and background events ($\times 10^4$) in the $Z \to ee$ channel after all selections, for an integrated luminosity of 50 pb^{-1}. The quoted uncertainties refer to the finite Monte-Carlo statistics only; systematic uncertainties are discussed in the text.
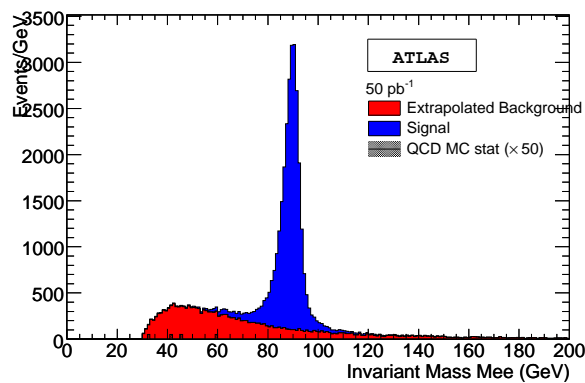

Figure 6: Di-electron invariant mass distribution in the $Z \to ee$ channel, for signal and background, for 50 pb^{-1}.

10

Background estimation.   As in the $W \rightarrow e\nu$ analysis, the simulation-based jet background estimate of Table 5 is replaced by a data-driven estimate. In this analysis, the signal and background fractions are estimated simultaneously, *via* a fit to both contributions. The signal is described by the convolution of a Breit-Wigner and a Gaussian resolution function, and the background, completely dominated by jet events, by an exponential function.

At the preselection level (just ahead of the electron identification), the background largely dominates the signal and allows to determine the exponential slope. After all cuts, the fit yields a background fraction of $(8.5 \pm 1.5)\%$, or $B = (0.23 \pm 0.04) \times 10^4$ events. The uncertainty on the background fraction derives from the modelling of the signal and background shapes.

The relatively important background rate is explained by the rather loose identification cuts. The present selections are chosen to illustrate the robustness of the signal extraction, and to exemplify the background extraction method.

4 Muon final states

4.1 $W \rightarrow \mu\nu$

Event selection.   The $W \rightarrow \mu\nu$ signal is selected as follows. The events should contain exactly one muon track candidate, passing the mu20 trigger item and satisfying $|\eta| < 2.5$ and $p_T > 25$ GeV. The energy deposited in the calorimeter around the muon track, within a cone of radius $\Delta R = 0.4$, is required to be lower than 5 GeV. The event missing transverse energy should satisfy $\not{E}_T > 25$ GeV, and $M_T > 40$ GeV is required.

For the initial luminosity the p_T cut of the trigger on the muon track is expected to be 20 GeV. Having a higher p_T threshold, however, can further reduce the backgrounds in particular from heavy flavour hadron decays and from decays in flight of long lived particles. The isolation, $\not{E}_T$ and M_T cuts are also effective to reduce those backgrounds.

After all selections, the overall efficiency for the signal is expected to be close to 80%, with very large rejection factors for $b\bar{b}$ and $t\bar{t}$ events. The number of events that are expected to pass the selection criteria for an initial luminosity of 50 pb^{-1} are shown in table 6. The expected background level corresponds to a fraction of $\sim 7\%$. Figure 7 shows the corresponding W transverse mass distribution before the transverse mass cut before the last cut of table 6.

Selection	$W \rightarrow \mu\nu$	$W \rightarrow \tau\nu$	$Z \rightarrow \mu\mu$	$b\bar{b} \rightarrow \mu X$	$t\bar{t}$
Trigger	44.44 ± 0.07	1.53 ± 0.01	2.03 ± 0.01	83.34 ± 0.09	0.53 ± 0.07
$p_T > 25\,\mathrm{GeV}, |\eta| < 2.5$	35.55 ± 0.06	1.22 ± 0.01	1.62 ± 0.01	68.27 ± 0.08	0.42 ± 0.06
Isolation	34.80 ± 0.06	1.20 ± 0.01	1.59 ± 0.01	9.67 ± 0.03	0.35 ± 0.06
$\not{E}_T > 25$ GeV	28.59 ± 0.05	0.72 ± 0.01	1.10 ± 0.01	1.00 ± 0.01	0.30 ± 0.05
$M_T > 40$ GeV	28.03 ± 0.05	0.57 ± 0.01	1.10 ± 0.01	0.10 ± 0.01	0.24 ± 0.05

Table 6: Number of expected signal and background events ($\times 10^4$) in the $W \rightarrow \mu\nu$ channel, for an integrated luminosity of 50 pb^{-1}. The quoted uncertainties refer to the finite Monte-Carlo statistics.
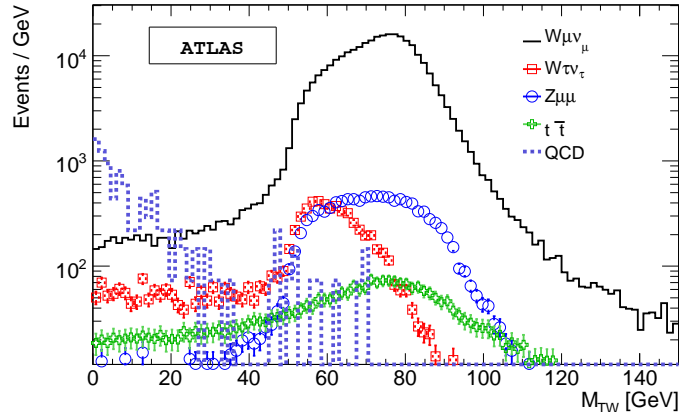
Figure 7: Transverse mass distribution in the $W \to \mu \nu$ channel, for signal and background, for 50 pb^{-1}.

Background estimation. Contrarily to the electron channels, the jet background is less important here and does not dominate the overall background. Muons from heavy flavour decays are rejected using the p_T and the isolation cuts, and muons from decays in flight of long lived particles could be further rejected using loose impact parameter cuts. The $t\bar{t}$ background and its uncertainty are small.

As can be seen in Table 6, the dominant backgrounds are expected from $W \to \tau \nu$ and $Z \to \mu \mu$ events. These processes are well understood theoretically, in particular with respect to the $W \to \mu \nu$ signal, and can be safely estimated based on simulation. A relative uncertainty of 3% is assumed on the $W \to \tau \nu$ background, as estimated from the experimental uncertainties on the W and τ branching fractions. Exploiting the CTEQ6.5 PDF sets (cf. Section 5), an uncertainty of 2% is assumed on the Z event rate passing the selections.

The jet background (mostly muons from b-hadron decays) is theoretically not well known. An uncertainty of 100% is assumed on this background component.

A theoretical uncertainty of about 15% on the $t\bar{t}$ cross-section is assumed. In addition, an uncertainty of 10% is considered on the rejection obtained from the isolation cut. This leads to a total uncertainty of about 20% on the $t\bar{t}$ background rate.

4.2 $Z \to \mu \mu$

Event selection. The $Z \to \mu \mu$ analysis uses the 10 GeV single muon trigger. The triggered data sample is further reduced by requiring at least two reconstructed muon tracks. The present analysis relies on the muon spectrometer only. The reconstructed muon tracks should satisfy $|\eta| < 2.5$ and $p_T > 20$ GeV. The reconstructed charges must be opposite, and the invariant mass of the muon pair is required to fulfil $|91.2 \text{ GeV-}M_{\mu\mu}| < 20$ GeV.

Muons in jet events tend to be produced within a decay cascade of further particles, and should therefore not appear isolated in the detector, in contrast to the leptonic decays of Z and W bosons. To quantify the isolation of the muons, the number of Inner Detector tracks within a cone around the
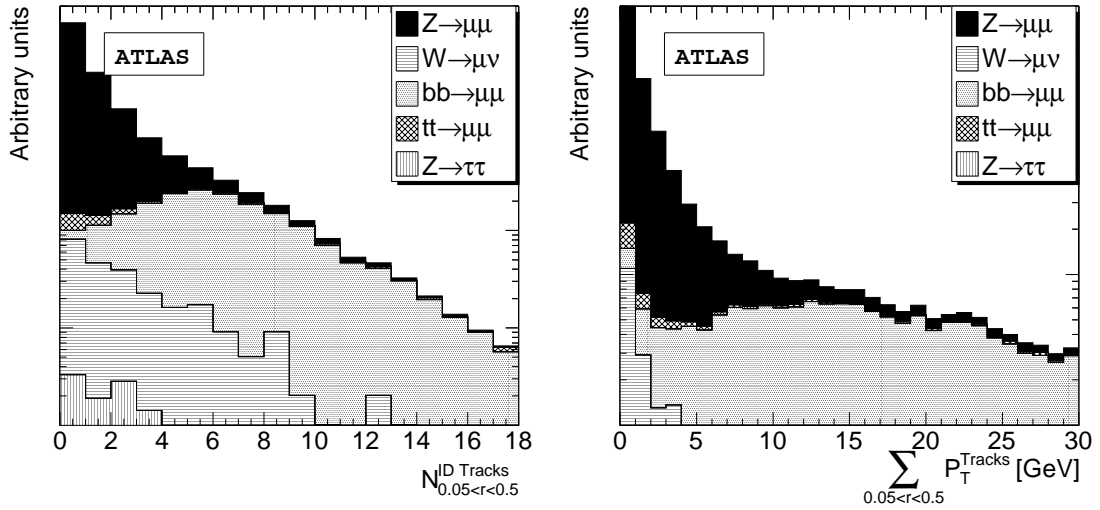
Figure 8: Distributions of the muon isolation variables for signal and backgrounds. Left : track multiplicity within $\Delta R = 0.5$ around the muon. Right : total transverse momentum of these tracks.

Selection	$Z \to \mu\mu$	$b\bar{b} \to \mu\mu X$	$W \to \tau\nu$	$Z \to \tau\tau$	$t\bar{t}$
Trigger	3.76 ± 0.01	10.08 ± 0.04	36.7 ± 0.1	0.09 ± 0.01	0.69 ± 0.01
2 muons +					
opp. charge	3.33 ± 0.01	3.00 ± 0.04	1.14 ± 0.02	0.04 ± 0.01	0.35 ± 0.01
$M_{\mu\mu}$ cut	3.04 ± 0.01	0.26 ± 0.01	0.04 ± 0.01	$(14 \pm 4) \times 10^{-4}$	0.02 ± 0.01
p_T cut	2.76 ± 0.01	0.125 ± 0.001	0.004 ± 0.001	$(11 \pm 4) \times 10^{-4}$	$(134 \pm 8) \times 10^{-4}$
Isolation	2.56 ± 0.01	$(18 \pm 5) \times 10^{-4}$	$(9 \pm 5) \times 10^{-4}$	$(11 \pm 4) \times 10^{-4}$	$(66 \pm 4) \times 10^{-4}$

Table 7: Number of expected signal and background events ($\times 10^4$) in the $Z \to \mu\mu$ channel, for an integrated luminosity of 50 pb^{-1}. The quoted uncertainties refer to the finite Monte-Carlo statistics.

candidate muon, as well as the total transverse momentum of these tracks are used. The cone size is $\Delta R = 0.5$, and the muon track itself is excluded from the calculation.

The distributions of the isolation variables for signal and background processes normalised to their cross sections is shown in Fig. 8, after the above-mentioned cuts.

The isolation and p_T cuts are chosen to minimise the statistical uncertainty on the cross-section measurement. The expected number of events after each cut are shown in Table 7. The chosen cuts select about 70% of the $Z \to \mu\mu$ events with muons in the detector acceptance. The residual background fraction of this selection is $0.004 \pm 0.001 (stat)$. The corresponding invariant mass distribution is shown in Fig. 9.

Background uncertainty. In this channel, the dominant background originates from $t\bar{t}$ events. Besides a theoretical uncertainty of about 15% on the cross-section, an uncertainty of 10% is assumed
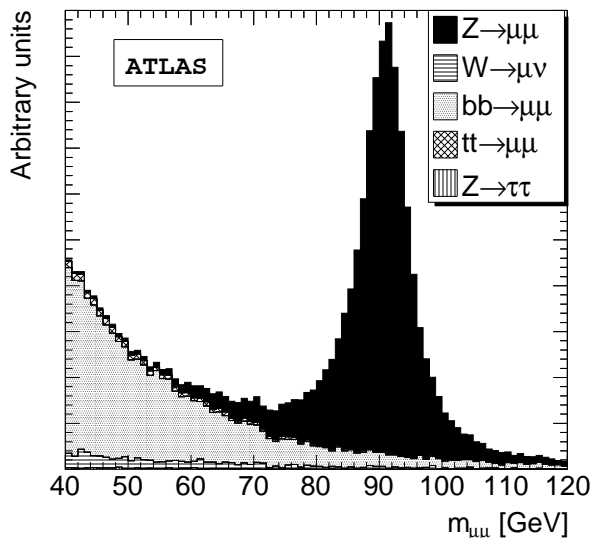
13

Figure 9: Di-muon invariant mass distribution in the $Z \rightarrow \mu\mu$ channel, for signal and background, for 50 pb^{-1}.

on the rejection obtained from the isolation cuts. This leads to a total uncertainty of about 20% on the $t\bar{t}$ background rate.

The jet background (mostly muons from b-hadron decays) is expected to be smaller, but is theoretically not well known. An uncertainty of 100% is assumed on this background component.
The other backgrounds are smaller, theoretically well known in comparison to the above, and contribute negligibly to the overall background uncertainty.

5 Common systematic uncertainties

5.1 Trigger and reconstruction efficiency

As has been seen in Sections 3 and 4, the selection of leptonic Z boson decays provides clean signals with low backgrounds. This allows to determine the lepton trigger [11, 12] and reconstruction efficiencies [8, 9] using the well-known tag-and-probe method, which is briefly outlined below.

Selecting $Z \rightarrow ee$ and $Z \rightarrow \mu\mu$ events as in Sections 3 and 4, *i.e.* requiring a single lepton trigger and two reconstructed leptons, the efficiency of a given trigger item is defined as the fraction of the selected events where the second reconstructed lepton passes this trigger item.

The off-line reconstruction efficiency can be determined in a similar way. Requiring one reconstructed lepton satisfying tight identification criteria, and requiring a second isolated, high-p_T object such that the invariant mass of the pair is close to the Z boson mass, provides a sufficiently pure $Z \rightarrow ll$ sample; the efficiency of a given identification criterion is then defined as the fraction of events where the second object is indeed identified. Conversely, the efficiency of the isolation cuts can be determined by requiring the second object to be identified, and counting the fraction of events where the isolation

14

cut is passed.

The above methods are exact in the limit where backgrounds vanish. For tight trigger and off-line cuts, this is the case in practice : the background magnitude and uncertainty have a negligible impact on the efficiency determination. Backgrounds are larger when assessing looser identification and isolation cuts, and lower trigger thresholds. In this case, interpreting the observed dilepton mass spectrum as a sum of signal and background contributions (described by the convolution of a Breit-Wigner resonance and a Gaussian resolution function, and by an exponential or polynomial function respectively) allows to extract the background fraction and correct the computation accordingly. This procedure was performed and shown to provide efficiency estimates that are unbiased within the statistical precision expected for $\mathscr{L} = 50 \text{ pb}^{-1}$.

Figures 10 and 11 illustrate this discussion, on the examples of the `e20` trigger item and Medium electron identification cut, and of the `mu20` trigger item and combined muon reconstruction. For the selections used in the analyses of Section 3 and 4, the overall efficiency can be reconstructed with a precision of $\delta\varepsilon/\varepsilon = 0.02$ for electrons and muons.

The overall reconstruction efficiencies in Fig. 10, 11 reflect the performance of the reconstruction software at the time of writing this note. Improved performance and results are presented in [8, 9, 11, 12].

5.2 Theoretical systematic uncertainties

This section presents comparisons on the acceptance for $W \to l\nu$ and $Z \to ll$ events, as obtained from the `Pythia`, `Herwig` and `MC@NLO`. The purpose of this study is to determine the contribution of the uncertainties on the acceptance to the overall systematic uncertainty on the cross-section.

The kinematic cuts described in Sections 3 and 4 are applied to the generator-level particles for each of the above generators. For W events, the acceptance varies by 2.5% from one program to the other. For Z events, we observe a variation of 3.2%.

The sources which could explain the observed differences are the Initial State Radiation (ISR), the intrinsic k_T for the incoming partons, the Underlying Event (UE), final state photon radiation, Parton Density Functions (PDFs) and matrix element corrections applied to the parton shower (ME).

To quantify the impact of the individual sources, samples are generated with ISR, k_T, UE and ME all switched off. For this configuration, important differences remain for the acceptances. The acceptance ratio between Pythia and Herwig is about 85.0 ± 0.4 % for W events and 101.6 ± 0.3% for Z events.

The effects of electroweak corrections on the acceptance have been studied using `PHOTOS`. By running alternatively with and without `PHOTOS`, one obtains an effect of 1.8% for W events and 2.8% for Z events.

Switching on ISR, or changing the intrinsic k_T of the incoming partons has an important impact on the η and p_T distributions. Specifically, ISR introduces a difference of 10.2% and 2.8% on the acceptance for W and Z events, respectively. ISR only affects `PYTHIA`, and not `HERWIG`. Similarly, turning on and off the k_T, ME and UE, the following differences on the acceptance are obtained: 1.9% (0.50%) for
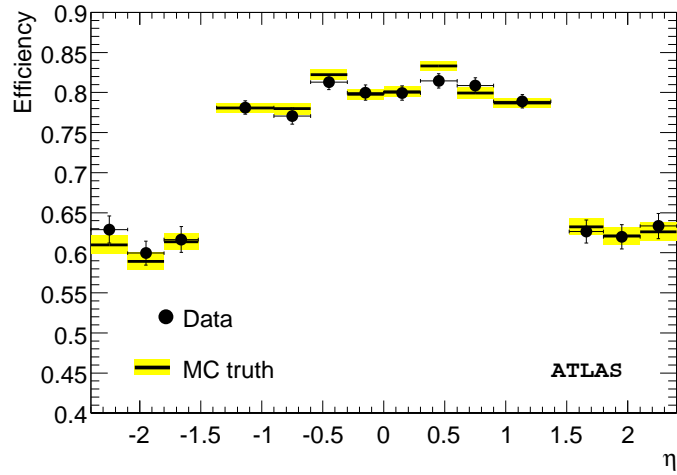
Figure 10: Electron detection efficiency vs. η, as measured from the tag-and-probe method and compared to the truth, for 50 pb^{-1}. The product of the e20 trigger efficiency, and Medium electron identification efficiency is represented.
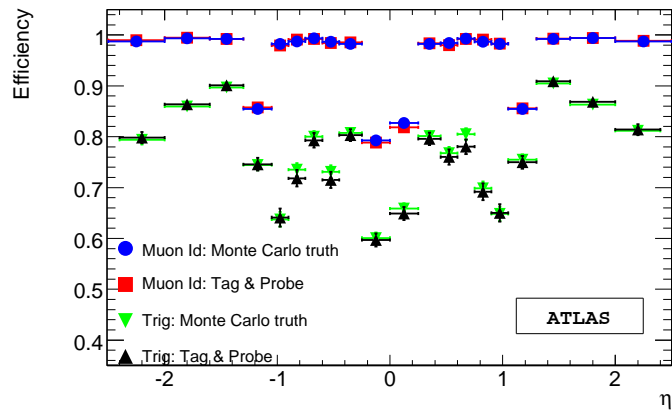

Figure 11: Muon detection efficiency vs. η, as measured from the tag-and-probe method and compared to the truth, for 50 pb^{-1}. The mu20 trigger efficiency, and the combined muon reconstruction efficiency are represented.

the intrinsic k_T, 1.0% (0.2%) for the UE and no effect for the ME.

For these sources, the systematic uncertainty is estimated as 20% of the above numbers, which amounts to assuming that the models describing the above are correct within 20%. One thus obtains the following errors for W→ $e\nu$: 2.0% (ISR), 0.4% (kT) and 0.2% (UE). In the case of PHOTOS, one has an error of 0.3%.

The PDFs are an important source of differences in the acceptances. The uncertainty is determined using the CTEQ6.5 PDF uncertainty sets. An uncertainty of 0.9% is found, for both W and Z events.

The total relative systematic uncertainty, calculated from the quadratic sum of all numbers, is $\delta A/A = 2.3\%$ for W events. Repeating the same exercise with Z events gives a total relative systematic uncertainty of $\delta A/A = 1.1\%$. While these uncertainties will be significantly reduced with the analysis of the LHC data, we assume these figures hold for our initial cross-section measurements.

6 Total cross-sections

Cross-section results for $\mathscr{L} = 50$ pb^{-1} are presented first. At the end of the section, the performance is extrapolated to higher luminosity.

6.1 Results for $\mathscr{L} = 50$ pb^{-1}

We gather below the results of the analyses performed in Sections 3 and 4, and of the discussion of systematic uncertainties of Section 5. Table 8 contains our estimations of statistical and systematic uncertainties, the cross-section values and their uncertainties computed according to Equations 2 and 3.

Process	$N(\times 10^4)$	$B(\times 10^4)$	$A \times \varepsilon$	$\delta A/A$	$\delta\varepsilon/\varepsilon$	σ (pb)
$W \to e\nu$	22.67 ± 0.04	0.61 ± 0.92	0.215	0.023	0.02	$20520 \pm 40 \pm 1060$
$W \to \mu\nu$	30.04 ± 0.05	2.01 ± 0.12	0.273	0.023	0.02	$20530 \pm 40 \pm\ \ 630$
$Z \to ee$	2.71 ± 0.02	0.23 ± 0.04	0.246	0.011	0.03	$2016 \pm 16 \pm\ \ \ 72$
$Z \to \mu\mu$	2.57 ± 0.02	0.010 ± 0.002	0.254	0.011	0.03	$2016 \pm 16 \pm\ \ \ 64$

Table 8: Measured cross-sections and their uncertainties, for an integrated luminosity of 50 pb^{-1}. The uncertainty on N is statistical, the other sources are systematic. The quoted cross-section uncertainties include the mentioned statistical and systematic contributions. An overall luminosity uncertainty of $\delta\mathscr{L}/\mathscr{L} = 10\%$ should be counted in addition.

As can be seen from Table 8, the results are dominated by the systematic error, even for $\mathscr{L} = 50$pb^{-1}. The luminosity uncertainty is common to all cross-sections, and vanishes in cross-section ratios, e.g σ_W/σ_Z. In the W channels, the systematic uncertainty is dominated by the background uncertainty. This can be expected given the important fraction of jet events. This background could be further reduced, notably by requiring the absence of jets, but this would jeopardize the inclusive nature of the cross-section measurement. The efficiency and acceptance uncertainties give a slightly smaller contribution.

The Z channels benefit from smaller backgrounds, due to the presence of two decay leptons. For the same reason, the efficiency uncertainty is also larger than in the W channels. Given the smaller acceptance uncertainty, the efficiency uncertainty is the largest source of uncertainty.

6.2 Prospects for $\mathscr{L} = 1$ fb^{-1}

For higher integrated luminosity, the statistical uncertainty on the counting (N) becomes negligible, and the efficiency uncertainty, which is determined from measurement and also of statistical nature, strongly decreases.

With increased luminosity, a number of modifications will have to be applied to the analyses. Most prominently, in the electron channels, the single electron trigger threshold will be increased to 22 GeV, and the Tight electron identification is expected to be used. In $Z \to \mu\mu$ channel, spectrometer muons are replaced by combined muons, and the muon isolation cuts are refined by exploiting calorimetric information in addition to the track-based isolation used in the low-luminosity analysis. The $W \to \mu\nu$ analysis is unchanged.

Table 9 summarizes the expected signal yields and the cross-section determination in this case. On this timescale, $\mathscr{L}$ might be measured with improved precision, exploiting elastic proton scattering at very small angles [14]. Compared to the low-luminosity analysis, the systematic uncertainties from backgrounds and efficiency are expected to scale with statistics. Without further input, the acceptance uncertainty does not decrease and dominates the result.

Process	$N (\times 10^5)$	$B (\times 10^5)$	$A \times \varepsilon$	$\delta A / A$	$\delta \varepsilon / \varepsilon$	σ (pb)
$W \to e\nu$	45.34 ± 0.02	1.22 ± 0.41	0.215	0.023	0.004	$20520 \pm \ 9 \pm 516$
$W \to \mu\nu$	60.08 ± 0.02	4.02 ± 0.05	0.273	0.023	0.004	$20535 \pm \ 7 \pm 480$
$Z \to ee$	5.42 ± 0.01	0.46 ± 0.02	0.246	0.011	0.007	$2016 \pm \ 4 \pm \ 27$
$Z \to \mu\mu$	5.14 ± 0.01	0.02 ± 0.001	0.254	0.011	0.007	$2016 \pm \ 4 \pm \ 27$

Table 9: Measured cross-sections and their uncertainties, for an integrated luminosity of 1 fb^{-1}. The uncertainty on N is statistical, the other sources are systematic. The quoted cross-section uncertainties include the mentioned statistical and systematic contributions. An overall luminosity uncertainty of $\delta \mathscr{L} / \mathscr{L} = 10\%$ should be counted in addition.

7 Differential cross-sections

As it is clear from the previous sections, total cross-section measurements are dominated by the systematic uncertainty even for modest integrated luminosity. The main cross-section uncertainty is related to the acceptance uncertainty, which in turn comes from our limited knowledge of the underlying physics (notably non-perturbative mechanisms and PDFs). It is therefore important to measure the distributions, which will help to constrain these uncertainties. Three examples are given below, namely the measurement of the Drell-Yan invariant mass spectrum at low mass, and the rapidity and transverse momentum distributions for Z events.

Compared to the inclusive analyses, the differential measurements require a larger statistics. For this reason the differential distributions shown in this Section refer to an integrated luminosity of 200 pb^{-1}, which corresponds to the available statistics of the Monte Carlo signal samples.

7.1 Low-mass Drell-Yan production

Event Selection. The selection criteria used to identify Drell-Yan di-electron pairs are summarised below. Two trigger channels are used for this study: the low threshold, single electron trigger e10, possible at low luminosity, and the double electron trigger 2e10 more adapted to higher luminosity. Beyond the trigger requirements, electron candidates are required to pass the Medium identification flag, and at least one of them must also satisfy the track matching and E/p identification cuts; exactly two such electrons are required, oppositely charged, each satisfying $p_T > 10$ GeV and $|\eta| < 2.5$. Finally, the missing transverse energy ($\not{E}_T$) in the event should be smaller than 30 GeV. Table 10 shows the impact of these cuts on signal and background.

The e10 trigger channel provides a global signal efficiency of about 4.5%; the efficiency reaches 51% at high mass, and is about 1% at electron pair mass $M = 8$ GeV. The 2e10 efficiency is much smaller, about 0.5% on average. In both trigger channels, the p_T threshold induces a significant distortion of the spectrum. This distortion is obviously more pronounced in the 2e10 channel.

cut	$\gamma^* \to ee$	$\tau\tau$	$t\bar{t}$	di-boson	jets
pre-selections	330912±575	69864±477	131924±233	7270±23	$10^{11} \pm 10^7$
Medium, $|\eta| < 2.5$	51003±226	557±45	3306±34	1142±11	$10^7 \pm 10^6$
$p_T > 10$ GeV	21112±145	409±34	2068±28	1125±11	$10^6 \pm 10^5$
$\not{E}_T < 30$ GeV	20903±145	329±34	307±11	841±11	$10^6 \pm 10^5$
e10 trigger	17107±131	324±34	284±11	824±11	$10^5 \pm 10^5$

Table 10: Signal and background event rates, following the selections described in the text, for 284 pb^{-1} integrated luminosity.

Background uncertainty. With the exception of inclusive jet events, contributions from all other background processes listed in Table 10 are estimated from simulation, by counting background events that pass through the selection criteria described above.

Due to the insufficient jet statistics available, this background contribution cannot reliably be calculated from simulation. It is assumed that a data-driven subtraction method based on the use of electron variables (like for instance those shown in Fig. 4 and 5), would have a similar performance in this analysis, as the data driven method described in Section 3, and leave only a negligeable jet contribution to the overall background.
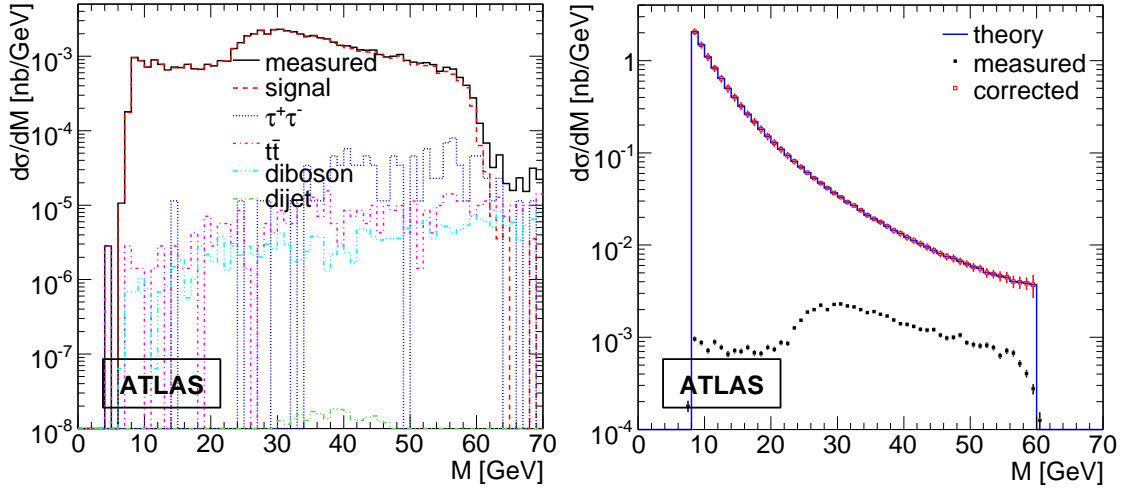
Figure 12: Left: Mass distribution of the signal (upper histogram) and of the backgrounds. In decreasing numerical importance: the $\tau\tau$, $t\bar{t}$, di-boson (ZZ, WZ and WW) and di-jet contributions. Right: Differential cross-section as a function of the mass of the pair. Lower histogram: raw event count. The upper histograms represent the measured cross-section (dots with error bars) and the true value as predicted by the simulation (line).

Results. After all selections, the signal cross-section is estimated in each mass bin according to Eq. 2, modified to account for the differential measurement presented here:

$$\left(\frac{d\sigma}{dM}\right)_i = \frac{N_i - B_i}{\varepsilon_i A_i \Delta M_i \mathscr{L}} \tag{4}$$

where N_i is the number of signal events in mass bin i, B_i is the number background events, ε_i the overall efficiency accounting trigger, identification and further selections. ΔM_i is the width of bin i and $\mathscr{L}$ represents the integrated luminosity.

The resulting Drell-Yan pair mass spectrum is displayed in Fig. 12 (left) including the main background species. The observed threshold in the signal mass spectrum is due to the thresholds of the `e10` and `2e10` triggers. Backgrounds are very small, representing less than 1% of the selected sample. It is mostly composed of Drell-Yan tau pairs. The jet background contribution is assumed to be small; this assumption is in agreement with the findings of Section 3 but would require explicit study.

The selected sample of events are corrected in two steps: first the estimated background subtracted from the observed event count, then the remaining events are corrected for the overall cut efficiency and acceptance, estimated from the signal simulation. Figure 12 (right) illustrates the procedure.

The integrated cross-section is calculated by integrating the corrected histogram; the error on the cross-section is estimated by adding the error of each bin in quadrature. Hence, the total Drell-Yan cross section in electron channel for the pair mass range between 8 GeV and 60 GeV is $\sigma_{\text{DY}} = 9.22$ nb. A conservative estimate of the statistical errors for two luminosity hypotheses are 7.3% for L = 50 pb^{-1} and 1.6% for L = 1 fb^{-1}.

Category i	Definition	n_i
1	All events	398 750
2	Fiducial and kinematics (generation)	172 544
3	Trigger and off-line (fiducial, kinematics and ID)	49 754
4	Intersection of categories 2 and 3	48 436

Table 11: Event categories used for the extraction of detector smearing corrections, geometric acceptance and event selection efficiency in the electron channel.

The invariant mass resolution, about 1 GeV, is found to have no considerable effect on the Drell-Yan spectrum. Further systematic uncertainties come from the trigger resolution and trigger pre-scaling have not been studied. One of the largest systematic uncertainty on the spectrum is the uncertainty due to parton distribution functions (PDFs). By studying the spectrum in this low mass region, the goal is to improve the precision of the PDFs. Finally, the acceptance correction is very large in this channel and needs to be controlled in sufficient detail.

7.2 Z differential cross-section : bin by bin correction method

Electron channel. In the electron channel, only events that pass the `2e12i` trigger condition are considered. Furthermore, it is required that they contain exactly two, oppositely charged electrons, each of them satisfying $|\eta| < 2.5$ and $P_T > 20$ GeV. Both electrons are required to pass the Tight electron identification criteria.

The background is dominated by hadrons misidentified as electrons in inclusive jet events. Taking into account that with the Tight identification criteria the expected rate of hadrons misidentified as electrons is very low (see [8]) the background remaining after the Tight selection criteria is also very low and can be neglected in the following.

After all selections, the following event categories are defined. In the following, n_1 denotes the total sample size; n_2 is the number of events having two generator-level electrons satisfying $|\eta| < 2.5$, $p_T > 20$ GeV, and 75 GeV $< M_{ee} < 105$ GeV. The number of events satisfying these conditions at the reconstruction level is noted n_3; finally, n_4 counts the events passing these criteria on both generation and reconstruction levels. Table 11 summarises these definitions and contains values for the n_i, directly counted from the simulated signal sample.

Muon channel. In the muon channel, only events that pass the `mu20` trigger condition are considered. The events should further contain exactly two oppositely charged muons, each of them satisfying $|\eta| < 2.5$. Both muons should be reconstructed in the Inner Detector and in the Muon Spectrometer. The most energetic muon should satisfy $p_T > 20$ GeV; the second one should have $p_T > 15$ GeV. The muon pair invariant mass should lie between 76 and 106 GeV.

Contamination from $W \rightarrow \mu\nu$ and $t\bar{t}$ events effectively disappears after the selection process, but $b\bar{b} \rightarrow \mu\mu$ contamination is still about 3.5% of the signal. To minimise the $b\bar{b}$ background, two isola-
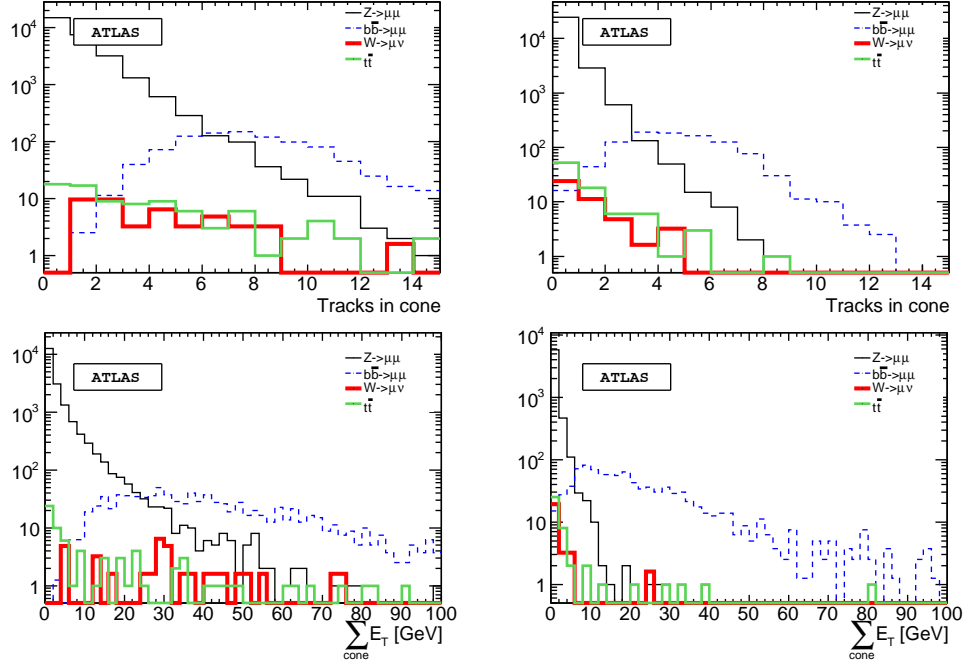
Figure 13: Number of tracks (top) and calorimeter E_T in a cone R = 0.45 (bottom). Distributions for the muon with the higher value of the quantity is shown on the left, and distributions for the muon with the lower value of the quantity on the right. Black: $Z \rightarrow \mu\mu$, red: $W \rightarrow \mu\nu$, blue: $b\bar{b} \rightarrow \mu\mu$, green: $t\bar{t}$.

tion quantities are studied. The first one is the number of tracks in a cone of size $\Delta R = 0.45$ around the muon track ; the second one is the total calorimeter transverse energy in the same cone. The distributions of these two quantities for the four samples, corresponding to 40 pb^{-1} of integrated luminosity, are shown in Fig. 13. A muon track is accepted if the first isolation variable is less than six and the second isolation variable is less than 20 GeV. These cuts are applied to both muons in the event.

The isolation cut efficiency for the signal sample is larger than 98%, and the residual contamination is less than 0.5%. The sample is pure enough at this point that we can neglect the background contamination in the differential cross-section plots.

As in the electron channel, four event categories are defined to allow the computation of the differential cross-section. The categories and their sizes n_i are given in Table 12.

Extraction of $d\sigma_Z/dp_T dy$ The Z boson phase space is sliced in rapidity and transverse momentum regions, or bins. In each region, labeled α, the differential cross-section is obtained from the raw event count using the usual expression:

$$\sigma_\alpha = \frac{S_\alpha}{\mathscr{L}} \frac{d_\alpha - b_\alpha}{\varepsilon_\alpha A_\alpha}, \qquad (5)$$

Category i	Definition	n_i
1	All events	445650
2	Fiducial and kinematics (generation)	234610
3	Trigger and off-line (fiducial, kinematics and ID)	181652
4	Intersection of categories 2 and 3	180260

Table 12: Event categories used for the extraction of detector smearing corrections, geometric acceptance and event selection efficiency in the muon channel.
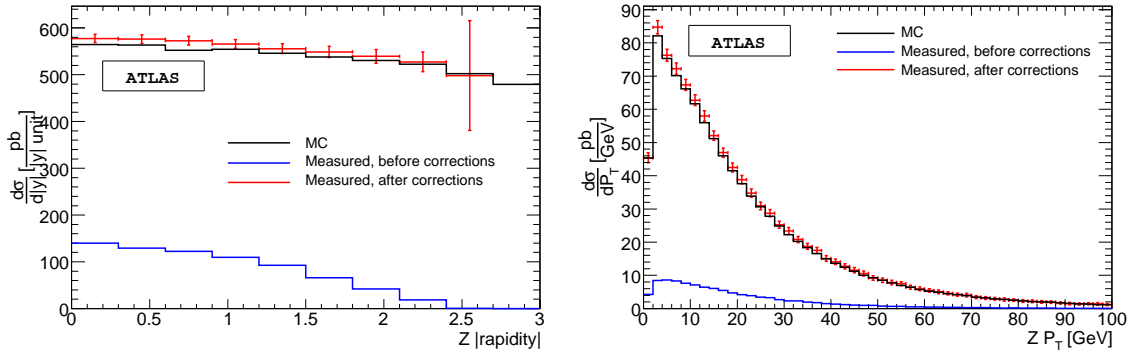

Figure 14: Left: $d\sigma_Z/dy$, integrated over p_T. Right: $d\sigma_Z/dp_T$, integrated over $-2.5 < y < 2.5$. Distributions obtained in the electron channel, with a precision corresponding to an integrated luminosity of 200 pb^{-1}.

where S_α, ε_α and A_α respectively represent the detector smearing correction (correcting for event migration to and from bin α, due to resolution effects), overall event selection efficiency and geometric acceptance in region α; d_α is the observed event count and b_α the estimated background in this region, and $\mathscr{L}$ is the integrated luminosity. In terms of the definitions in Section 7.2, we have:

$$S_\alpha = \frac{n_{3,\alpha}}{n_{4,\alpha}}, \quad \varepsilon_\alpha = \frac{n_{3,\alpha}}{n_{2,\alpha}}, \quad A_\alpha = \varepsilon_{filter}\frac{n_{2,\alpha}}{n_{1,\alpha}}, \quad d_\alpha = n_{3,\alpha}, \tag{6}$$

where the $n_{i,\alpha}$ are computed according as in Section 7.2, but in each bin α of the Z phase space. The acceptance values account for the generator-level filtering efficiency, as described in Section 2.2.

Differential cross-section results In the electron channel, the Z boson phase space was divided in 50 p_T bins and 6 rapidity bins. The p_T bins have a width of 2 GeV, in the range $0 < p_T < 100$ GeV. The rapidity intervals are defined as follows: [0, 0.3], [0.3, 0.6], [0.6, 0.9], [0.9, 1.2], [1.2, 1.6], and [1.6, 2.6]. The extracted differential cross-sections are illustrated in Fig. 14, in the form of p_T distributions for the various rapidity regions. A good agreement is observed between the reconstructed cross-sections and the true distributions, obtained from an idependent generator-level sample.

In the muon channel, the Z boson phase space was divided in 50 p_T bins and 9 rapidity bins. The p_T bins have a width of 2 GeV, in the range $0 < p_T < 100$ GeV. The rapidity bins have a width of 0.3, in the range $0 < |y| < 2.7$. Figure 15 shows the Z boson differential cross-section in the dimuon
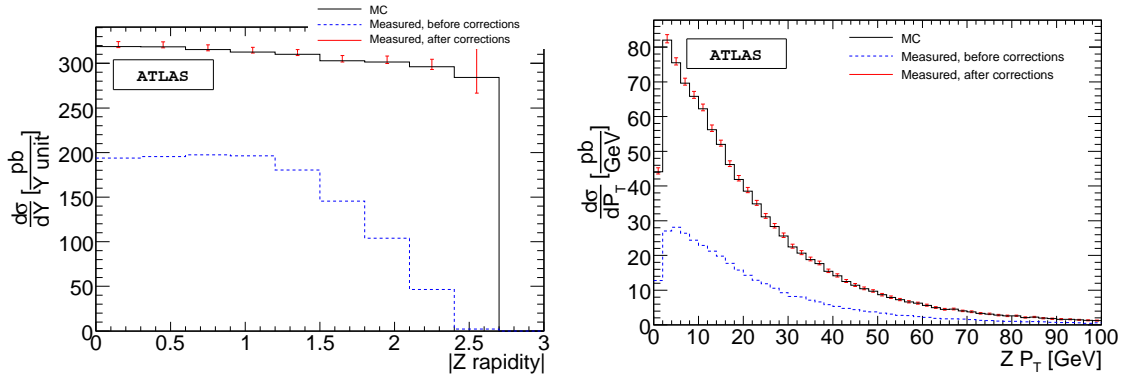
Figure 15: Left: $d\sigma_Z/dy$, integrated over p_T. Right: $d\sigma_Z/dp_T$, integrated over $-2.7 < y < 2.7$. Distributions obtained in the muon channel, with a precision corresponding to an integrated luminosity of 200 pb^{-1}.

channel in rapidity and transverse momentum bins. The black histograms correspond to the generated cross-section, the blue histograms to the measured cross-section before corrections are applied, while the red histograms show the measured cross-section after all corrections have been applied.

The plots have been normalised to the total NNLO cross-section of 2015 pb times a global acceptance factor of 0.73. Since the correction factors and measurement were both extracted from the same dataset, the good agreement between the black and red histograms is of course expected.

7.3 Z differential cross-section : alternative method

The method presented here attempts to fully exploit the phase space of the Z boson and its decay products. Writing the cross-section in terms of the complete phase space allows to extract, in addition to the Z boson distributions, possible p_T, η or ϕ dependencies of the lepton selection efficiency.

Method principle. The events are classified in bins both for the Z and for the decay leptons. We define N_{yZ} bins along y^Z, and N_{ptZ} bins along p_T^Z. As before, the Z boson phase space intervals are labelled α. In addition, we define N_{Et} intervals in the lepton transverse energy distribution, and N_η intervals for the leptons pseudorapidity. The lepton phase space is labelled i, j (one index for each lepton).

For each α, we measure N_{ij}^α, which is the number of lepton pairs reconstructed with one lepton in bin i and one lepton in bin j. The following relation holds, in the practical absence of background, as justified in the previous sections:

$$N_{ij}^\alpha = \varepsilon_i \varepsilon_j P_{ij}^\alpha \mathscr{L} \Delta\sigma^\alpha, \tag{7}$$

where P_{ij}^α is the probability, computed on Monte Carlo, that a Z boson produced in bin α decays into two leptons in bins i and j; ε_i is the lepton reconstruction efficiency in bin i; $\mathscr{L}$ is the integrated luminosity, and $\Delta\sigma^\alpha$ is the Z production cross-section in bin α.

Resolution effects, primarily on the lepton E_T, are accounted for as follows. When the P_{ij}^α histograms are filled, the lepton E_T is first smeared according to its expected, E_T and η dependent resolution. The smeared quantities are then used to compute the Z variables (p_t, y). In this way the above equation is unchanged and all detector effects can be incorporated in the P_{ij}^α factors. Writing the above for all α, i, j provides an over-constrained system whose unknowns are the efficiencies and cross-sections. We can then compute the ε_i in each bin α, up to a factor related to $\mathscr{L}\Delta\sigma^\alpha$.

The system can be solved analytically, using for example the singular value decomposition method, or SVD. A drawback of this method is that it is based on least squares; it is thus not valid in the case of low statistics. In particular, at low luminosity, the statistics are such that several bins contain only a few events. To avoid bias in the efficiency determination, a likelihood using Poisson probabilities is constructed and used to fit the efficiencies numerically. In order to help the fit to converge, we first solve the system using the SVD method, and we use the results as initial parameters of the fit. Since the ε_i are expected not to depend on α, we can compute their weighted average over the bins α.

In case of low statistics, the bin sizes should be large enough to integrate a sufficient statistics in each bin. If the lepton reconstruction efficiency is not constant within each bin, the hypothesis that the efficiency does not depend on the Z boson phase space might be violated. To avoid such effects, the lepton binning is chosen such that the efficiency is *a priori* constant within each bin. This results in bins with variable width, which doesn't affect the method.

In any given Z phase space interval α, we can write for each lepton bin (i, j) the following relation:

$$\mathscr{L}\Delta\sigma^\alpha = \frac{N_{ij}^\alpha}{<\varepsilon_i><\varepsilon_j> P_{ij}^\alpha}, \tag{8}$$

where $<\varepsilon_i>$ and $<\varepsilon_j>$ are the average efficiencies computed at the previous step. Finally, $\mathscr{L}\Delta\sigma^\alpha$ is computed by averaging over all (i, j).

"Classical limit" of the method. As was discussed above, the method proposed here has several limitations in the case of low statistics. It might need significant integrated luminosity to be applied safely. The classical method is reached by simply setting $N_{Et} = N_\eta = 1$, and accordingly computing the acceptance and efficiencies from Monte-Carlo in each Z boson phase space interval α.

Resolution effects are taken into account as before, by smearing the Monte Carlo input before determining the acceptance. Once the acceptance and efficiency are determined in each bin α, just counting the number of events N^α in the bin and allows to deduce the differential cross-section using the usual cross-section expression in the absence of background:

$$\mathscr{L}\Delta\sigma^\alpha = \frac{N^\alpha}{\varepsilon^\alpha \varepsilon^\alpha A^\alpha}. \tag{9}$$

Results. The complete method has been tested on the $Z \to \mu\mu$ samples described in Section 2.2. Due to the limited statistics, the Z phase space was mapped using N_{ptZ} =10 for $0 < p_T^Z < 60$ GeV, N_{yZ} =5 for $2.5 < y^Z < 2.5$. The muon reconstruction efficiency has no p_T-dependence above 10 GeV; this allows to set N_{Et} =1. The definition of the muon η intervals is dictated by the detector geometry which affects the efficiency as a function of η; we set N_η =7, with the intervals [-2.7,-1.6], [-1.6,-1.4],
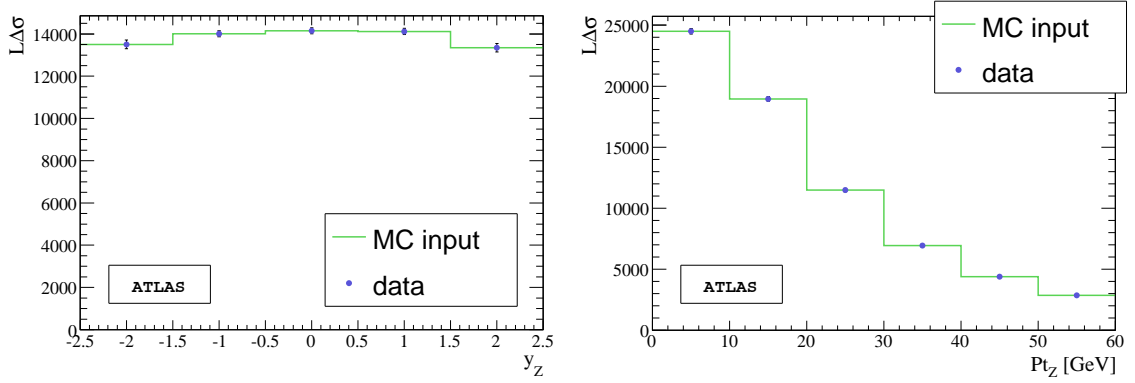
Figure 16: Left: $\mathscr{L}\Delta\sigma$ versus y^Z, integrated over p_T^Z. Right: $\mathscr{L}\Delta\sigma$ versus p_T^Z, integrated over y^Z.
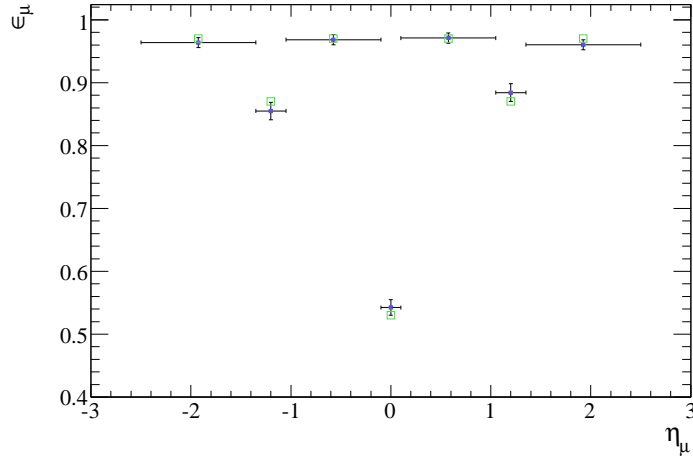

Figure 17: Muon reconstruction efficiency versus η, measured simultaneously with the differential cross-section.

[-1.4,-0.1], [-0.1,0.1], [0.1,1.4], [1.4,1.6], [1.6,2.7].

The results are illustrated in Fig. 16. The Z boson rapidity and p_T distributions are correctly reconstructed. Measured and true distributions agree within the statistical precision, which varies from 3% in regions where the differential cross-section is high, to about 20% in the tails of the Z boson phase space ($y^Z > 1.5$). In addition, the η dependence of the reconstruction efficiency can be measured accurately. Given the interval definition above and the size of our sample, a precision of about 2% is obtained for each point. This is competitive with the tag-and-probe determination described in Section 5, and illustrated in Fig. 17.

For cross-checks, the classical limit of the method has been tested using the $Z \to ee$ samples. The intervals are defined as before, except $N_{yZ} = 10$ and $N_{ptZ} = 20$. The following selection criteria are applied: two reconstructed electrons of opposite charge are required in the detector acceptance ($|\eta| \geq 2.5$), with $20\ GeV \leq p_t \leq 80\ GeV$. Both electrons should pass the Tight identification flag. Z events are
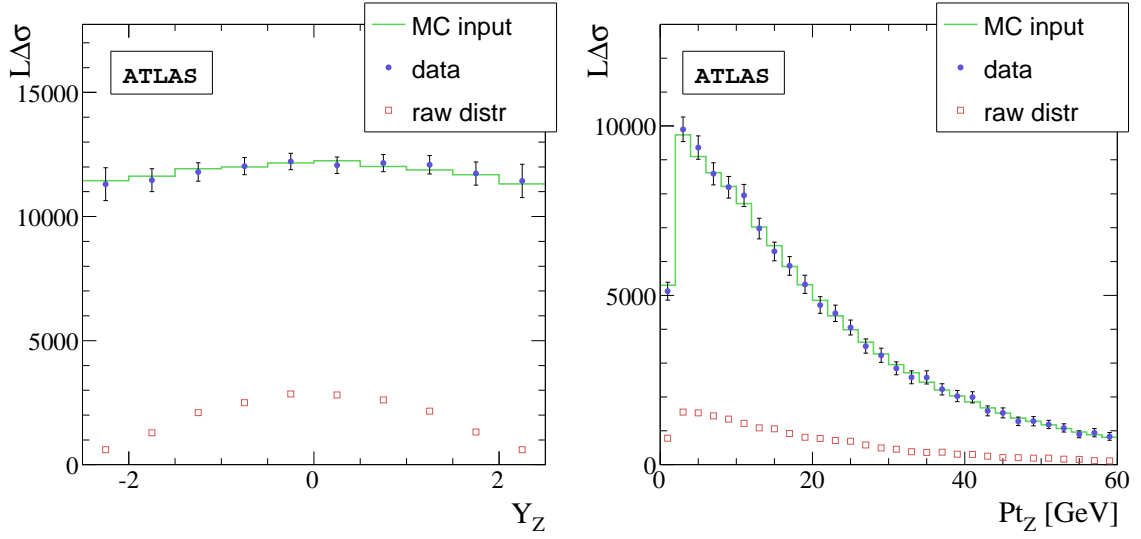
Figure 18: Left: $\mathscr{L}\Delta\sigma$ versus y^Z, integrated over p_T^Z. Right: $\mathscr{L}\Delta\sigma$ versus p_T^Z, integrated over y^Z.

selected around the masse peak ($87\ GeV \leq M_Z \leq 95\ GeV$), with $p_T^Z \leq 60\ GeV$. The acceptance cuts on the electrons imply $y^Z \leq 2.5$.

The results of the differential cross-section $d\sigma/dy^Z$, integrated over p_T^Z, and $d\sigma/dp_T^Z$, integrated over $y^Z$are shown in Fig. 18. The squares represent the raw distribution, the dots represent the measurements, corrected by the acceptance and the efficiency factors. The shows the input value. The measurements are consistent with the input, which validates the method.

8   Summary and perspectives

This work presents the ATLAS prospects for the measurement of W and Z boson cross-sections at the LHC. In the four considered channels ($W \to e\nu$, $Z \to ee$, $W \to \mu\nu$, $Z \to \mu\mu$), the analyses confirm the high purity of the samples after fairly usual selections (high-p_T lepton identification, isolation, and $E\!\!\!/_T$ in the W final states). The jet background is poorly predicted, and dedicated studies are needed to monitor its magnitude using real data. Data-driven methods are presented that seem to have sufficient sensitivity to keep the jet background at a level where it does not prevent a precise cross-section measurement.

With 50 pb^{-1}, the background and signal acceptance uncertainties contribute similarly to the measured cross-section uncertainty, at the level of 2-4% depending on the channel. Extrapolating to 1 fb^{-1}, all uncertainties are expected to scale with statistics, except the acceptance uncertainty. This then leads to the usual conclusion [?] that the W and Z cross-sections can not be measured to a precision better than about 2 %.

This argument however ignores the additional input from differential cross-section measurements. Contrarily to total cross-sections, the differential ones benefit from small acceptance uncertainties,

and have the potential to constrain the uncertainties that affect total cross-sections. The examples of the dilepton mass spectrum below the Z peak, and of the Z boson rapidity and p_T distributions are studied here. The methods presented here are shown to provide correct estimations of the differential cross-sections. The natural next step of these analyses, *i.e.* quantify their physical implications, is beyond the scope of this note and reserved for the real data.

References

[1] T. Sjostrand, S. Mrenna and P. Skands, JHEP **05**, 026 (2006).

[2] K. Melnikov and F. Petriello, Phys. Rev. **D74**, 114017 (2006).

[3] S. Frixione and B. R. Webber, JHEP **06**, 029 (2002).

[4] M.Schott, *Matthias Schott thesis*

[5] J. Pumplin et al., JHEP **07**, 012 (2002).

[6] A. Rimoldi et al., *ATLAS detector simulation: Status and outlook*, Prepared for 9th ICATPP Conference on Astroparticle, Particle, Space Physics, Detectors and Medical Physics Applications, Villa Erba, Como, Italy, 17-21 Oct 2005.

[7] ATLAS Collaboration, *ATLAS reference cross-sections*, this volume.

[8] ATLAS Collaboration, *Electron Reconstruction Performance*, this volume.

[9] ATLAS Collaboration, *Muon Reconstruction Performance*, this volume.

[10] ATLAS Collaboration, $\not{E}_T$ *Missing Trasnsverse Energy Reconstruction Performance*, this volume.

[11] ATLAS Collaboration, *Electron Trigger performance*, this volume.

[12] ATLAS Collaboration, *Muon Trigger performance*, this volume.

[13] ATLAS Collaboration, *ATLAS detector description*

[14] ATLAS Collaboration, *Luminosity project*